THE JOURNAL OF PHYSICAL CHEMISTRY Letters

Letter

pubs.acs.org/JPCL

Operando EPR for Simultaneous Monitoring of Anionic and Cationic Redox Processes in Li-Rich Metal Oxide Cathodes

Mingxue Tang,[†,‡] Annalisa Dalzini,[‡] Xiang Li,[†] Xuyong Feng,[†] Po-Hsiu Chien,[†] Likai Song,[‡] and Yan-Yan Hu*[,†,‡]

[†]Department of Chemistry and Biochemistry, Florida State University, Tallahassee, Florida 32306, United States

[‡]National High Magnetic Field Laboratory, 1800 East Paul Dirac Drive, Tallahassee, Florida 32310, United States

Supporting Information

ABSTRACT: Anionic redox chemistry offers a transformative approach for significantly increasing specific energy capacities of cathodes for rechargeable Li-ion batteries. This study employs operando electron paramagnetic resonance (EPR) to simultaneously monitor the evolution of both transition metal and oxygen redox reactions, as well as their intertwined couplings in Li_2MnO_3, $Li_{1.2}Ni_{0.2}Mn_{0.6}O_2$, and $Li_{1.2}Ni_{0.13}Mn_{0.54}Co_{0.13}O_2$ cathodes. Reversible O^{2-}/O_2^{n-} redox takes place above 3.0 V, which is clearly distinguished from transition metal redox in the operando EPR on Li_2MnO_3 cathodes. O^{2-}/O_2^{n-} redox is also observed in $Li_{1.2}Ni_{0.2}Mn_{0.6}O_2$, and $Li_{1.2}Ni_{0.13}Mn_{0.54}Co_{0.13}O_2$ cathodes, albeit its overlapping potential ranges with Ni redox. This study further reveals the stabilization of the reversible O redox by Mn and e^- hole delocalization within the Mn−O complex. The interactions within the cation−anion pairs are essential for preventing O_2^{n-} from recombination into gaseous O_2 and prove to activate Mn for its increasing participation in redox reactions. Operando EPR helps to establish a fundamental understanding of reversible anionic redox chemistry. The gained insights will support the search for structural factors that promote desirable O redox reactions.

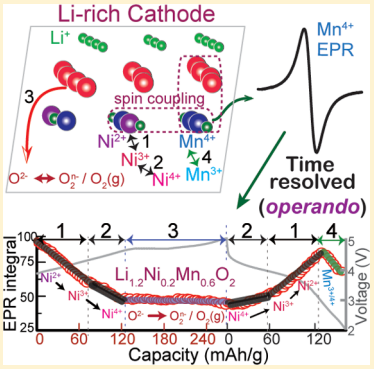

To meet the ever-growing demand for energy storage technologies with high energy and power density, the search for suitable cathodes for rechargeable Li-ion batteries (LIBs) continues.[1−3] Layered manganese-based materials with large specific capacity and high voltage represent the state-of-the-art.[4−7] Li-rich materials LMO (with M being the combination of Mn and Mg, Al, P, Co, Ni, and/or Ru), such as Li_2MnO_3, $Li_{1.2}Ni_{0.2}Mn_{0.6}O_2$ (LNMO), and $Li_{1.2}Ni_{0.13}Mn_{0.54}Co_{0.13}O_2$ (LNMCO), have attracted tremendous research effort to sustain their high capacities beyond the first cycle. To further extend the frontier of designing high-energy cathode materials, new chemistry is needed to enable additional capacity beyond what transition metal (TM) redox can offer. Recent discussions have explored the possibility of employing reversible anionic redox reactions to create higher capacity at high voltages. Oxygen (O) redox was used in Li−O_2 and Li−air batteries, but the performance was compromised due to the challenges in stabilizing desirable redox products.[5,8] The combination of TM with O redox can lead to synergy for providing the following benefits: (1) capacity harvested from both TM and O redox reactions; (2) TM-stabilized O redox products by sharing d orbitals to accommodate e^- loss and gain and prevent irreversible O_2 evolution and the associated structural degradation. For instance, Tarascon et al. proposed that the introduction of 4d and 5d TMs in $Li_2Ru_{1-y}SnyO_3$[9] and $LiIrO_3$[10] can attain capacities up to 230 and 170 mAh/g for many cycles, respectively. These TMs can stabilize the structure during cycling and reduce the possibility of O_2 loss. The big question is whether we could adopt the design principles from these expensive model systems for more practical cathodes, such as the Mn-based Li-rich materials, which deliver high energy density at a relatively low price.

In the past two years, extensive efforts have been directed toward understanding the mechanism of O redox reactions in Li-rich cathodes. It was claimed that, in addition to partial O_2 gas release proposed by earlier investigations,[11−14] electron holes formed on the oxygen sites,[15,16] which may lead to reversible e^- insertion and extraction and contribute to extra reversible capacity. The new mechanism cast the promise that reversible O redox for enhanced energy density in Li-rich cathodes is possible if the local structure can be stabilized to prevent O_2 formation.[17,18] Ceder and co-workers used density functional theory (DFT) calculation[15] to unveil the chemical and structural features that lead to reversible O redox and thus extra capacity. Their study concluded that labile electrons could be extracted from orphaned oxygen states created with the Li−O−Li configuration in Li-excess cathode materials. Bruce et al.[16] applied differential electrochemical mass spectrometry (DEMS), Raman spectroscopy, and X-ray absorption near-edge structure (XANES) to confirm that a small amount of O_2 was formed upon charging the $Li_{1.2}Ni_{0.13}Mn_{0.54}Co_{0.13}O_2$ (LNMCO) cathode above 4.5 V, but mainly electron holes were formed at

Received: June 5, 2017
Accepted: August 10, 2017
Published: August 10, 2017

DOI: 10.1021/acs.jpclett.7b01425
J. Phys. Chem. Lett. 2017, 8, 4009−4016

4.5 V. Additionally, there was no O_2^{2-} generation during cycling LNMCO, verified with Raman spectroscopy. An operando X-ray absorption study on the LNMCO cathode found that both TMs (Ni and Co) and O were involved in the reversible redox reactions, but no redox reaction was associated with Mn.[19] The O−O dimers in layered cathodes were visualized via transmission electron microscopy (TEM) and neutron diffraction (ND).[20] The role of metal substitutes for stabilizing $(O_2)^{n-}$ against O_2 recombination in Li-rich phases was also discussed. The release of O_2 in Li-rich cathodes has been widely studied by both experimental[11,12,16,21−30] and DFT[15,30−32] efforts. The collective results, despite debates on the detailed mechanisms, showed that electron holes were formed first and then O−O was dimerized to form O_2; O_2 release led to structural destabilization and phase separation, which in turn caused the capacity fading after the first charge.[33]

A delicate balance exists between reversible O redox for enabling extra capacity and O_2 recombination and release causing capacity fading in Li-rich cathodes. A path needs to be found to stabilize the O redox against O_2 formation, and TMs are expected to play an important role in this process. A better understanding of the TM−O complex and its evolution during cycling of the Li-rich cathodes is critical. Electron paramagnetic resonance (EPR) is capable of determining the local configurations of different TMs and spin interactions among them.[34−39] Furthermore, EPR can easily detect peroxo-like species in layered cathodes.[9] Recently, EPR spectroscopy and imaging has been employed to probe the Li mossy structure and radical formation of working batteries.[40−42]

Operando EPR, with high detection sensitivity, is a powerful tool to simultaneously follow the evolution of cationic TM and anionic O redox reactions during battery operation. In this contribution, a quantitative operando EPR protocol is devised to probe cation−anion redox correlation in real time. Li_2MnO_3 is chosen as the model material to reveal the evolution of $Mn^{3+/4+}$, together with $O^{2-}/(O_2)^{n-}$ redox. Then, the study is extended to two complex materials, $Li_{1.2}Ni_{0.2}Mn_{0.6}O_2$ (LNMO) and $Li_{1.2}Ni_{0.13}Mn_{0.54}Co_{0.13}O_2$ (LNMCO), to determine the coexisting interactions among different TMs and the roles of different TMs in stabilizing the reversible O redox process.

Figure 1 demonstrates the setup for operando EPR observation of LMO/Li batteries, where LMO represents Li_2MnO_3, $Li_{1.2}Ni_{0.2}Mn_{0.6}O_2$, or $Li_{1.2}Ni_{0.13}Mn_{0.54}Co_{0.13}O_2$. The picture of a bag cell battery is shown in Figure 1a with the schematic of its configuration to the right. The high-voltage Li-rich cathode and Li metal anode are separated by a piece of glass fiber, which contains the electrolyte LP30. Both electrodes are closely attached to Ti-mesh current collectors. The entire battery is located in the center of the EPR cavity (Figure 1b) and connected to an external galvanostat for electrochemical operation. The orientation of the bag cell battery relative to the magnetic field strongly affects the EPR signal intensity due to magnetic susceptibility. Spectra of batteries at different orientations with respect to the magnetic field are shown in Figure S2. In all of the following experiments, the battery cell is oriented in parallel with the external magnetic field, $\mathbf{B}_0$, to maximize detection sensitivity and ensure consistency. Figure 1c presents CW-EPR spectra of different components in a LMO/Li battery and their combinations. From bottom to top are EPR spectra of pure LMO, LMO mixed with conductive carbon additive, Li metal, and a pristine LMO/Li half-cell battery, respectively. L_2MnO_3 powder shows a broad symmetric signal, which is mainly from the antiferromagnetically coupled

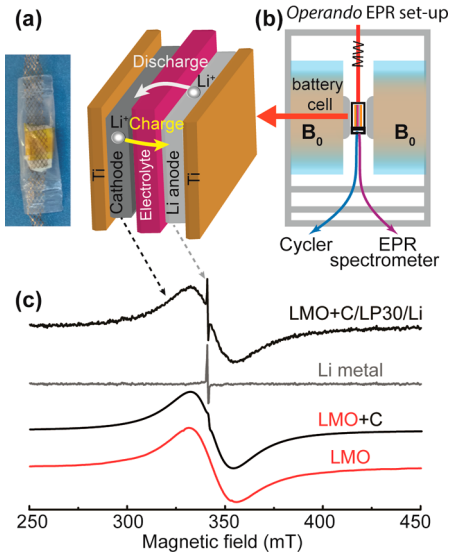

Figure 1. (a) Picture and schematic of a LMO/Li half-cell battery for operando EPR studies, containing a Li-rich cathode and a Li metal anode, which are separated by a piece of glass fiber soaked with LP30 electrolyte. The whole battery is located in the center of the resonator cavity of an EPR spectrometer (b), with a connection to a galvanostat for electrochemical operation. (c) CW-EPR spectrum of the pristine battery and its constituents, pure LMO, LMO mixed with conductive additive, and Li metal. LMO represents Li_2MnO_3, $Li_{1.2}Ni_{0.2}Mn_{0.6}O_2$, or $Li_{1.2}Ni_{0.13}Mn_{0.54}Co_{0.13}O_2$.

Mn^{4+}−O cluster. The Mn^{4+}−O EPR signal exhibits a single Lorentzian line shape centered at $g \approx 2.00$.[34] The addition of conductive acetylene black leads to a very weak sharp peak, which is attributed to delocalized electrons. Similarly, conductive Li metal shows a relatively sharp peak, with a g value of 2.00. EPR signatures for both the LMO cathode and Li anode are observed for a pristine LMO/Li battery. Deconvolution of the spectrum from a LMO/Li battery shown in Figure S3 clearly distinguishes contributions from LMO and Li, respectively. The above foundation work establishes the basis for operando EPR to simultaneously monitor changes associated with both cathodes and Li metal anodes.

Figure 2 presents the CW-EPR spectra of three Li-rich cathode materials, Li_2MnO_3, LNMO, and LNMCO. The EPR

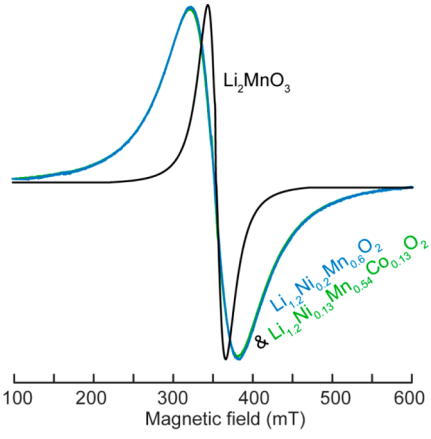

Figure 2. CW-EPR spectra of pristine Li_2MnO_3, $Li_{1.2}Ni_{0.2}Mn_{0.6}O_2$, and $Li_{1.2}Ni_{0.13}Mn_{0.54}Co_{0.13}O_2$ samples.

DOI: 10.1021/acs.jpclett.7b01425
J. Phys. Chem. Lett. 2017, 8, 4009−4016

resonance of Li_2MnO_3 is relatively narrow with a single Lorentz-governed line shape, showing a peak-to-peak width of 22 mT, consistent with previous reports.[34] The latter two samples, LNMO and LNMCO, show almost identical broad spectra of a Lorentzian shape. The observed EPR signal mainly comes from Mn^{4+}. The additional broadening of LNMO and LNMCO spectra, compared with the Li_2MnO_3 spectrum, is associated with ferromagnetic correlation between Ni^{2+} and Mn^{4+} ions.[43,44] Ni^{2+}−O−Mn^{4+} has weak ferromagnetic interactions, Ni^{3+}−O−Mn^{4+} exhibits moderate antiferromagnetic couplings, and Ni^{4+}−O−Mn^{4+} often shows very strong antiferromagnetic interactions. These differences in their magnetic interactions with Mn^{4+} enable indirect EPR detection of Ni redox at room temperature. Similarly for Co, Co^{4+}−Mn^{4+} antiferromagnetic interaction is much stronger than Co^{3+}−Mn^{4+}, which allows the indirect EPR monitoring of Co^{3+}/Co^{4+} redox. Therefore, the different couplings between Mn−O, Mn−Ni, and Mn−Co form the basis for probing both TM and O redox processes using operando Mn^{4+} EPR at room temperature.

Operando EPR is first applied to follow the evolution of redox reactions within a Li_2MnO_3/Li battery. Upon charging, Li ions are extracted from Li_2MnO_3 and deposited on the Li anode. As shown in Figure 3, the Li metal EPR peak grows during charge.[40] The increased intensity is due to lose deposition of Li onto the Li metal anode,[40] which allows the microwave to penetrate with minimal skin depth effects. On the other hand, smooth dense deposition would not change the EPR signal intensity due to skin depth effects.[41] To test the EPR signal dependence on the specific surface area, EPR experiments were performed for two Li foils with the same mass but different surface roughness. The foil with a rough surface shows much more intense EPR signal compared to the one with a smooth surface (Figure S4). The discharge process strips Li from the Li anode and reintercalates it into the Li_2MnO_3 electrode. A gradual decrease of the EPR signal is observed for Li metal. This reflects that Li removal from the Li anode mainly takes place from the newly formed loose surface instead of the bulk Li anode. The EPR signal from the cathodes also evolves with the charge−discharge process. The following discussion will focus on the quantitative changes associated with anionic and cationic redox reactions in LMO cathodes.

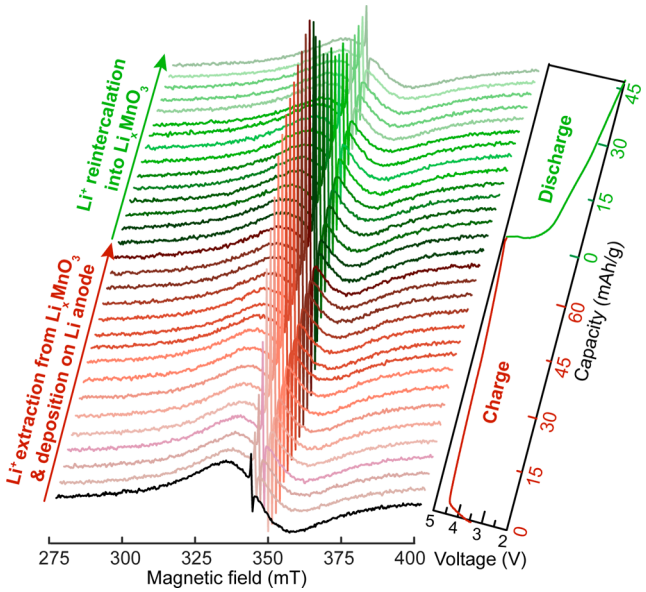

Figure 3. Selective operando CW-EPR spectra of a Li_2MnO_3/Li half-cell battery together with the electrochemical profile for the first charge−discharge cycle.

The electrochemical profile of a Li_2MnO_3/Li half-cell battery as a function of capacity is presented in Figure 4a with the dQ/dV plot shown in Figure S5. During the first charge−discharge cycle, 0.33 Li is extracted per Li_2MnO_3 unit upon charge, and 0.21 Li is reintercalated into Li_2MnO_3 upon discharge. During the second cycle, 0.48 Li is extracted from Li_2MnO_3 upon charge, and 0.31 Li is reintercalated upon discharge. The increased capacity following the first activation cycle was also previously observed for Li_2MnO_3.[14] It is worth noting that the specific capacities obtained for the three chosen LMO cathodes are not optimized to the best reported values in the literature due to the limitation of the battery cell containers required for the operando characterizations. Nevertheless, they encompass all of the electrochemical processes in LMO cathodes and satisfy the purpose of this study, which is to demonstrate a quantitative method for real time and simultaneous monitoring of anionic and cationic redox reactions.

Li_2MnO_3 is a neat system to start with because it does not involve complications induced by the coexistence of other TMs. In order to obtain quantitative information regarding the evolution of operando EPR spectra of the Li_2MnO_3/Li cell battery, the integral of the Mn^{4+} EPR resonance is calculated, and the results are shown in Figure 4b. The integral of the Li_2MnO_3 cathode EPR signal increases at the very beginning of charge (0−0.03 Li) (Figure 4b) because the residual Mn^{3+} in pristine Li_2MnO_3 with defects is oxidized to Mn^{4+}. The Mn^{4+} signal remains constant during further charge (0.03−0.33 Li), indicating no redox activities associated with Mn at this stage. The 0.30 Li extraction should be accompanied by the removal of e^- from O^{2-} to maintain electroneutrality, leading to electron hole formation on the O atom or ultimate release of O_2 gas.[7−9] Therefore, the capacity gained here (0.03−0.33 Li) is mainly associated with O^{2-} oxidation in the range of 4.5−5.0 V. The products of O^{2-} oxidation have been reported to be O_2^{n-} (n = 0, 1, 2, or 3).

The Mn^{4+} EPR integral decreases during the first discharge, which is attributed to the reduction of Mn^{4+} (Figure 4b).[45,46] The slope of the Mn^{4+} signal loss changes at ∼3.0 V, suggesting that Mn^{4+} is reduced in different manners above and below 3.0 V, and this kink point marks the transition from one form of Mn^{4+} reduction to the other. Direct reduction of $Mn^{4+} \rightarrow Mn^{3+}$ often occurs below 3.0 V. The decrease of Mn^{4+} EPR signal above 3.0 V is likely through an O-mediated Mn^{4+} reduction process; the O^{2-} oxidation product, O_2^{n-} (n = 1, 2 and 3), formed during the first charge, is stabilized by Mn^{4+}. During discharge above 3.0 V, e^- will be harvested first by O_2^{n-}. Through Mn−O spin coupling, Mn^{4+} is apparently reduced, leading to a reduction in the Mn^{4+} EPR signal.

A bilinear increase in the Mn^{4+} EPR integral is observed for the second charge, with $Mn^{3+} \rightarrow Mn^{4+}$ oxidation below 3.0 V and $O^{2-} \rightarrow O_2^{n-}/O_2(g)$ oxidation above 3.0 V. The second discharge exhibits a similar bilinear pattern, but with slightly increased capacity compared with the first discharge.

Quantification results also reveal that at least 1/3 of the O redox reaction is reversible, with the remaining irreversibly forming $O_2(g)$. It is worth noting that the Mn^{4+} EPR intensity dropped to ∼50% of the original amount at the end of the first discharge and to 30% at the end of the second discharge,

DOI: 10.1021/acs.jpclett.7b01425
J. Phys. Chem. Lett. 2017, 8, 4009−4016

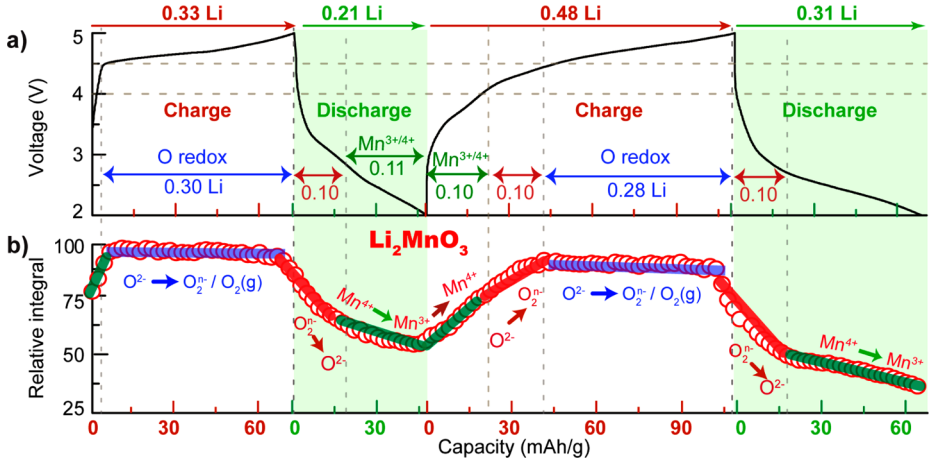

Figure 4. (a) Electrochemical profile of a Li_2MnO_3/Li half-cell battery as a function of specific capacity. (b) Evolution of the EPR signal integral from the Li_2MnO_3 cathode in a Li_2MnO_3/Li half-cell battery. The color coding distinguishes different redox processes: $Mn^{4+} \leftrightarrow Mn^{3+}$ (green), O redox at the plateau (blue), and reversible $O^{2-} \leftrightarrow O_2^{n-}$ below the plateau (red).

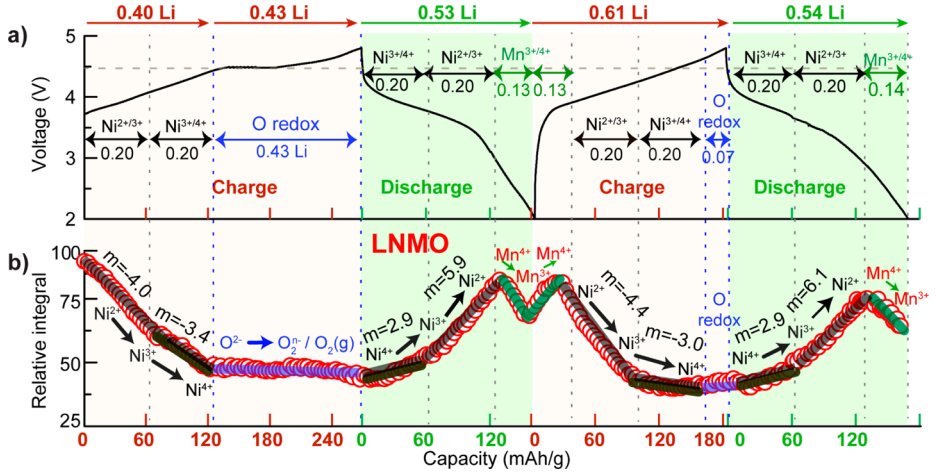

Figure 5. (a) Electrochemical profile of a LNMO/Li half-cell as a function of specific capacity. (b) Evolution of the EPR integral on the LNMO cathode within a LNMO/Li half-cell battery. The color coding distinguishes different redox processes: $Ni^{2+} \leftrightarrow Ni^{3+}$ (gray), $Ni^{3+} \leftrightarrow Ni^{4+}$ (black), O redox (blue), and $Mn^{4+} \leftrightarrow Mn^{3+}$ (green).

suggesting increased Mn^{4+} participation in redox, leading to increased capacity in the second cycle. Controlled ex situ EPR experiments were also carried out for pristine and cycled Li_2MnO_3 (Figure S8) cathodes, and the results complement and confirm operando measurements.

The EPR signal integral of Li metal is also quantified. It increases linearly upon charge but with two different rates. As shown in Figure S11, two linear regions can be found, and the fitting results indicate that the EPR intensity at the very beginning of charge increases about 7 times faster than the one in the later period of charge. The amount of Li is expected to be deposited linearly with capacity. The different rate (slope) observed in the EPR integral evolution is attributed to varied density of deposited Li. Li is first loosely deposited onto the Li metal surface, and a microwave can efficiently penetrate into these newly formed Li microstructures. However, the later-arrived Li will fill into the pores in prior formed microstructures. This will cause a densification and slow down the growth of EPR signal due to skin depth effects. Similar trends are also observed in the subsequent cycles and for the LNMO/Li and LNMCO/Li systems (Figures S12 and S13). EPR intensity from Li decreases upon discharge (Figures S11, S12, and S13).

When other TMs in addition to Mn are incorporated into the LMO structure, more Li ions can be extracted in Li-rich cathodes due to the increased amount of TM with redox-active pairs per unit mass.[15,47,48] LNMO is a typical Li-rich cathode material for LIBs. The added Ni^{2+} in LNMO can be easily oxidized to Ni^{4+}.[11] The electrochemical profile of a LNMO/Li half-cell battery is shown in Figure 5a. The first stage of charge allows 0.4 Li to be extracted, accompanied by $Ni^{2+} \rightarrow Ni^{4+}$ oxidation. Within the voltage range from 4.5 to 4.8 V, an additional 0.43 Li is extracted from LNMO; accordingly, electrons should be removed from O^{2-} in LNMO, leaving electron holes on O or resulting in O_2 release. The first discharge reintercalates 0.53 Li into LNMO with e^- contributed to Ni^{4+}, Mn^{4+}, and $(O_2)^{n-}$ reduction reactions. In the second charge−discharge cycle, 0.61 Li is extracted from the cathode, and 0.54 Li is subsequently reintercalated.

Multiple TM-involved redox reactions in conjunction with anionic redox processes greatly increase the complexity of the mechanisms for generating high capacity in Li-rich electrodes. The capability of operando EPR in directly probing changes

DOI: 10.1021/acs.jpclett.7b01425
J. Phys. Chem. Lett. 2017, 8, 4009−4016

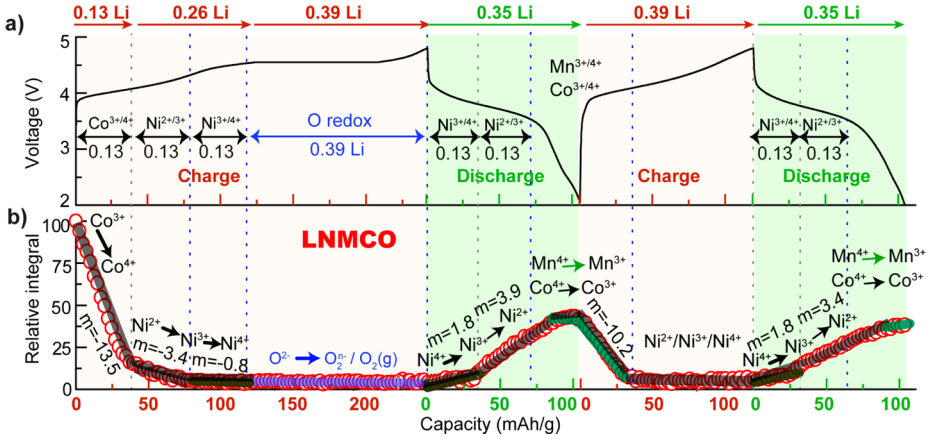

Figure 6. (a) Electrochemical profile of a LNMCO/Li half-cell battery as a function of specific capacity. (b) Evolution of the EPR integral on the LNMCO cathode within a LNMCO/Li half-cell battery. The color coding distinguishes different redox processes: $Ni^{2+} \leftrightarrow Ni^{3+}$ and $Co^{3+} \leftrightarrow Co^{4+}$ (gray), $Ni^{3+} \leftrightarrow Ni^{4+}$ (black), O redox (blue), and $Mn^{4+} \leftrightarrow Mn^{3+}$ (green).

associated with Mn^{4+} and indirectly detecting variations in Ni and O based on their couplings to Mn^{4+} allows the disentanglement of the complex puzzle. EPR signal evolution of the LNMO cathode is shown in Figure S10, and the quantification results are presented in Figure 5b. For the pristine battery, EPR-active Mn^{4+} shows a strong signal, which is broadened by Mn^{4+}–Ni^{2+} coupling. Upon charging, Ni^{2+} is oxidized to Ni^{3+} and then to Ni^{4+}. The Ni^{3+} and Ni^{4+} ions decrease the Mn^{4+} EPR intensity significantly (Figure 5b). This is attributed to increased antiferromagnetic couplings between Mn^{4+} and Ni^{3+}/Ni^{4+} ions, which quenches EPR signal in the X-band.[49,50] The decreasing rate of the EPR signal changes between $Ni^{2+} \rightarrow Ni^{3+}$ and $Ni^{3+} \rightarrow Ni^{4+}$ oxidation regions. During the second region of charge, from 4.5 to 4.8 V, as marked in blue in Figure 5b, the integral of the Mn^{4+} signal remains nearly constant, indicating no oxidation state change for Ni or Mn. The required e^- extraction has to originate from O^{2-} to form O_2^{n-} or $O_2(g)$.

The first discharge reinserts Li into LNMO, accompanied by the reduction of O_2^{n-}, Ni^{4+}, and Mn^{4+}. As shown in Figure 5b at the beginning of discharge (>4.0 V), the EPR signal grows very slowly due to the competing effects of O_2^{n-} and Ni^{4+} reduction on Mn^{4+}. On one hand, O_2^{n-} reduction will reduce the Mn^{4+} EPR signal, as observed in the case of Li_2MnO_3. On the other hand, the reduction of Ni^{4+} releases the "paired-coupling" between Mn^{4+} and Ni^{4+}, a reverse process of the charging, and thus will increase the Mn^{4+} EPR signal. Below 4.0 V, the signal grows faster and linearly. Ni^{4+} is reduced to Ni^{2+} in the range of 3.2–4.0 V, as shown in the dQ/dV plot (Figure S6).[45,51] Further discharge below 3.2 V produces a reduction in the EPR integral because Mn^{4+} (EPR-active) is reduced to Mn^{3+} (EPR-silent). At the beginning of the second charge, the EPR integral increases as a result of $Mn^{3+} \rightarrow Mn^{4+}$ oxidation. Further charge oxidizes Ni^{2+} to Ni^{4+}, resulting in the re-emergence of Mn^{4+}–Ni^{4+} coupling and Mn^{4+} EPR signal reduction. The initial increase followed by a decrease in the EPR signal suggests that $Mn^{3+} \rightarrow Mn^{4+}$ oxidation is followed by $Ni^{2+} \rightarrow Ni^{4+}$. A quasi-plateau in the Mn^{4+} EPR signal growth is observed between 4.0 and 4.5 V of the second charge, which indicates a mixed O^{2-} and Ni^{3+} oxidation. The e^- removal from O^{2-} and subsequent hole delocalization increase the apparent amount of Mn^{4+}. The decrease in the EPR signal as a result of Ni^{3+} oxidation is partially offset by the increase yielded from O^{2-} oxidation and e^- hole delocalization; thus, the quasi-plateau is shown. The very small plateau at >4.5 V is a result of O_2 evolution, which bears no effect on the Mn^{4+} EPR. During the second discharge, Ni^{4+} and O_2^{n-} reductions precede the reduction of $Mn^{4+} \rightarrow Mn^{3+}$, reminiscent of the first discharge.

To further demonstrate the capability of operando EPR for probing cationic and anionic redox in complex Li-rich cathodes, $Li_{1.2}Ni_{0.13}Mn_{0.54}Co_{0.13}O_2$ (LNMCO) is investigated. The electrochemical profile of a LNMCO/Li half-cell battery is shown in Figure 6a. The first stage of charge allows 0.39 Li to be extracted below 4.5 V, accompanied by Ni^{2+} oxidized to Ni^{4+} and Co^{3+} to Co^{4+} and possible e^- extraction from O^{2-}. Similar to LNMO, between 4.5 and 4.8 V, an additional 0.39 Li is extracted from LNMCO. It is worth mentioning that the number of Li ions extracted during this period is strongly dependent on the material synthesis, electrode making, and cycling conditions.[52] To maintain the charge neutrality, 0.39 e^- needs to be removed from O^{2-}. The first discharge reintercalates 0.35 Li into LNMCO. The second charge extracts 0.39 Li from the LNMCO cathode, and 0.35 Li is restored upon discharge.

For LNMCO, the broad EPR signal (Figure 6b) shows a steeper initial decay upon charge than that for LNMO due to the strong Co^{4+}–Mn^{4+} magnetic coupling.[53] The slope of the decrease is −13.5, compared with −4.0 obtained for the LNMO cathode at the initial state of charge. Unlike the operando X-ray-based method,[19] operando EPR can clearly distinguish Co and Ni redox processes. After $Co^{3+} \rightarrow Co^{4+}$ oxidation, the EPR signal decay slows down at ∼4.0 V, where $Ni^{2+} \rightarrow Ni^{3+}$ oxidation begins. Operando EPR can further discern the two processes, $Ni^{2+} \rightarrow Ni^{3+}$ and $Ni^{3+} \rightarrow Ni^{4+}$, by a change of decay rate at 4.3 V (Figure 6). The slowing down of the signal decay may also be partially due to O^{2-} oxidation and electron hole delocalization leading to an apparent increase in Mn^{4+}. Eventually, the broad EPR signal from LNMCO disappears completely and remains zero at and above 4.5 V (blue region), as shown in Figures 6 and S10. Upon discharge, a slow increase (black region) is observed initially due to $Ni^{4+} \rightarrow Ni^{3+}$ reduction, possibly accompanied by the reduction of O_2^{n-}. This slow growth region is followed by a linear increase due to reduction of $Ni^{3+} \rightarrow Ni^{2+}$. The relatively flat region (black and green) at the end of discharge is a result of mixed $Co^{4+} \rightarrow Co^{3+}$ and $Mn^{4+} \rightarrow Mn^{3+}$ reduction with opposite impact on the Mn^{4+} EPR intensity.

DOI: 10.1021/acs.jpclett.7b01425
J. Phys. Chem. Lett. 2017, 8, 4009–4016

Assuming that all electrons accompanying Li re-intercalation ions come from the reduction of $Ni^{4+} \rightarrow Ni^{2+}$ and $Co^{4+} \rightarrow Co^{3+}$, 90% (0.35/0.39) of the interactions among Ni^{2+}/Ni^{4+}, Co^{4+}, and Mn^{4+} should be removed, leading to about 90% recovering of the Mn^{4+} EPR signal. However, only 50% signal is recovered. This discrepancy suggests that the discharge should involve certain reduction of O_2^{n-} and $Mn^{4+} \rightarrow Mn^{3+}$, which is also confirmed from the dQ/dV plot with a second peak below 3.7 V (Figure S7). The $Mn^{4+} \leftrightarrow Mn^{3+}$ redox process of the LNMCO cathode is less obvious compared to that in the LNMO cathode; this is mainly due to competition and overlapping of several redox reactions. LNMCO EPR evolution in the second charge−discharge cycle resembles that of the first one, except that no irreversible O_2 evolution can be observed above 4.5 V during the second charge.

Among the three Li-rich cathode systems in this study, Li_2MnO_3 is very neat for a clean understanding of the roles that Mn and O play in the electrochemical processes. Mn^{4+} in pristine Li_2MnO_3 is not active upon the first charge; therefore, the 0.33 e^- (per Li_2MnO_3) accompanying Li^+ removal above 4.5 V is mainly extracted from O^{2-} to form $O_2^{n-}/O_2(g)$, confirmed by the nonchanging Mn^{4+} EPR signal. At the early stage of discharge above 3.0 V, electrons inject into O_2^{n-} first, and due to the Mn−O coupling, the Mn^{4+} EPR signal is reduced. Below 3.0 V during discharge, Mn^{4+} is reduced to Mn^{3+}, and the Mn^{4+} EPR signal continues to decrease but with a slower rate. The rate change in the operando EPR signal decay helps to distinguish the anionic and cationic redox processes in Li_2MnO_3. An estimate shows that 0.10 e^- is consumed for O_2^{n-} reduction and 0.11 e^- is used for $Mn^{4+} \rightarrow Mn^{3+}$ reduction, out of the total 0.21 e^- that accompanies Li^+ insertion during the first discharge. During the second charge, 0.20 e^- is removed below 4.5 V, and the increase in the Mn^{4+} EPR signal indicates that 0.10 e^- is removed from Mn^{3+} and 0.10 e from O^{2-}, which is stabilized by Mn; 0.28 e^- is taken out above 4.5 V, and no change in the Mn^{4+} EPR suggests that electrons are removed from O^{2-} to form more O_2^{n-} or $O_2(g)$. The removal of e^- from O^{2-} seems to help activate more Mn^{4+} to be reduced in the following discharge. This electron delocalization within the Mn−O complex is reflected by the change in the Mn^{4+} EPR signal when Mn is not directly involved in redox reactions at high voltages.

The operando EPR signal on LNMO shows a bilinear decrease for the $Ni^{2+} \rightarrow Ni^{3+} \rightarrow Ni^{4+}$ two-step oxidation at the early stage of the first charge. The decrease slows down at 4.0 V partially due to the reversible $O^{2-} \rightarrow O_2^{n-}$ oxidation. The relatively flat increase in the EPR signal at the beginning of first discharge is a result of competition between O reduction causing a decrease in the EPR signal and Ni reduction leading to an increase in the EPR signal. Once the O reduction process ceases, the increase of the EPR signal is faster as a result of $Ni^{3+} \rightarrow Ni^{2+}$ reduction. Below 3.0 V, $Mn^{4+} \rightarrow Mn^{3+}$ reduction takes place, resulting in the drop of the Mn^{4+} EPR signal. The Mn^{4+} EPR signal is recovered due to the $Mn^{3+} \rightarrow Mn^{4+}$ oxidation at the beginning of the second charge. Following a nearly linear decrease in the EPR signal induced by $Ni^{2+} \rightarrow Ni^{3+}$ oxidation, a quasi-plateau occurs at around 4.0 V instead of >4.5 V. This "early arrival" of the plateau is again a result of two competing processes, the reversible O oxidation to increase the signal and $Ni^{3+} \rightarrow Ni^{4+}$ oxidation to decrease the signal. The plateau in the EPR signal above 4.5 V is from O^{2-} oxidation to form $O_2^{n-}/O_2(g)$.

For the LNMCO cathode, operando EPR reveals that upon first charge $Co^{3+} \rightarrow Co^{4+}$ occurs below 4.0 V. Between 4.0 and 4.5 V, in addition to $Ni^{2+} \rightarrow Ni^{3+}$ and $Ni^{3+} \rightarrow Ni^{4+}$, reversible $O^{2-} \rightarrow O_2^{n-}$ oxidation takes place. Above 4.5 V, O^{2-} oxidation continues. Upon first discharge, reversible $O_2^{n-} \rightarrow O^{2-}$ reduction occurs above 4.0 V, followed by stepped $Ni^{4+} \rightarrow Ni^{3+} \rightarrow Ni^{2+}$ reductions and then $Co^{4+} \rightarrow Co^{3+}$. The reduction of $Mn^{4+} \rightarrow Mn^{3+}$ only happens below 3.0 V.

In summary, the quantitative operando EPR characterization of Li_2MnO_3, LNMO, and LNMCO has led to the following insights: (i) TM (Ni, Mn, Co) redox processes can be clearly distinguished in operando EPR, based on different magnetic interactions between Ni and Co of various oxidation states with Mn^{4+}; (ii) O−Mn coupling allows indirect probing of O redox, which can be discerned from cationic redox; (iii) reversible O redox occurs in all three Li-excess materials and is most clearly observed in Li_2MnO_3. Reversible O oxidation starts at voltages below the 4.5 V plateau and overlaps with Ni redox processes in LNMO and LNMCO; and (iv) Mn−O coupling stabilizes $(O_2)^{n-}$ and also activates more Mn^{4+} to participate in the redox reactions, and both effects help to increase cathode specific capacity.

Operando EPR has been successfully demonstrated for simultaneous monitoring of both cationic and anionic redox processes in Li-excess metal oxide cathode materials. The coupling between Mn and O is believed to create necessary synergy for stabilizing $(O_2)^{n-}$ species and also activating more Mn to participate in the electrochemical processes. Both factors yield gradually increased specific capacity. This work has established a convenient, inexpensive, and quantitative approach for probing reversible O redox and cationic redox processes at the same time. This approach will prove useful for advancing the understanding of anionic redox processes and promote the anionic redox mechanism by new materials design for increasing energy densities of rechargeable batteries beyond what cationic redox can offer.

■ ASSOCIATED CONTENT

Supporting Information

The Supporting Information is available free of charge on the ACS Publications website at DOI: 10.1021/acs.jpclett.7b01425.

Experimental details on sample preparation and operandoEPR measurements, together with Li anode integrals (PDF)

■ AUTHOR INFORMATION

Corresponding Author

*E-mail: hu@chem.fsu.edu.

ORCID

Mingxue Tang: 0000-0002-7282-4100

Notes

The authors declare no competing financial interest.

■ ACKNOWLEDGMENTS

This work was supported by Florida State University through Hu Startup and the National Science Foundation under Grant No. DMR-1508404. All EPR experiments were carried out at the NHMFL supported by NSF under Contract DMR-1157490. We thank Prof. Michael Shatruk for stimulating discussion on EPR data analysis.

DOI: 10.1021/acs.jpclett.7b01425
J. Phys. Chem. Lett. 2017, 8, 4009−4016

REFERENCES

(1) Tarascon, J.-M.; Armand, M. Issues and Challenges Facing Rechargeable Lithium Batteries. *Nature* **2001**, *414* (6861), 359−367.
(2) Armand, M.; Tarascon, J.-M. Building Better Batteries. *Nature* **2008**, *451* (7179), 652−657.
(3) Wagner, F. T.; Lakshmanan, B.; Mathias, M. F. Electrochemistry and the Future of the Automobile. *J. Phys. Chem. Lett.* **2010**, *1* (14), 2204−2219.
(4) Manthiram, A. Materials Challenges and Opportunities of Lithium Ion Batteries. *J. Phys. Chem. Lett.* **2011**, *2* (3), 176−184.
(5) Larcher, D.; Tarascon, J.-M. Towards Greener and More Sustainable Batteries for Electrical Energy Storage. *Nat. Chem.* **2014**, *7* (1), 19−29.
(6) Hy, S.; Liu, H.; Zhang, M.; Qian, D.; Hwang, B.-J.; Meng, Y. S. Performance and Design Considerations for Lithium Excess Layered Oxide Positive Electrode Materials for Lithium Ion Batteries. *Energy Environ. Sci.* **2016**, *9* (6), 1931−1954.
(7) Saubanère, M.; McCalla, E.; Tarascon, J.-M.; Doublet, M.-L. The Intriguing Question of Anionic Redox in High-Energy Density Cathodes for Li-Ion Batteries. *Energy Environ. Sci.* **2016**, *9* (3), 984−991.
(8) Bruce, P. G.; Freunberger, S. A.; Hardwick, L. J.; Tarascon, J.-M. Li-O2 and Li-S Batteries with High Energy Storage. *Nat. Mater.* **2011**, *11* (1), 19−29.
(9) Sathiya, M.; Rousse, G.; Ramesha, K.; Laisa, C. P.; Vezin, H.; Sougrati, M. T.; Doublet, M.-L.; Foix, D.; Gonbeau, D.; Walker, W.; et al. Reversible Anionic Redox Chemistry in High-Capacity Layered-Oxide Electrodes. *Nat. Mater.* **2013**, *12* (9), 827−835.
(10) Pearce, P. E.; Perez, A. J.; Rousse, G.; Saubanère, M.; Batuk, D.; Foix, D.; McCalla, E.; Abakumov, A. M.; Van Tendeloo, G.; Doublet, M.-L.; et al. Evidence for Anionic Redox Activity in a Tridimensional-Ordered Li-Rich Positive Electrode B-Li2IrO3. *Nat. Mater.* **2017**, *16* (5), 580−586.
(11) Armstrong, A. R.; Robertson, A. D.; Bruce, P. G. Overcharging Manganese Oxides: Extracting Lithium beyond Mn4+. *J. Power Sources* **2005**, *146* (1−2), 275−280.
(12) Armstrong, A. R.; Holzapfel, M.; Novák, P.; Johnson, C. S.; Kang, S.-H.; Thackeray, M. M.; Bruce, P. G. Demonstrating Oxygen Loss and Associated Structural Reorganization in the Lithium Battery Cathode Li [Ni0. 2Li0. 2Mn0. 6] O2. *J. Am. Chem. Soc.* **2006**, *128* (26), 8694−8698.
(13) Croy, J. R.; Park, J. S.; Dogan, F.; Johnson, C. S.; Key, B.; Balasubramanian, M. First-Cycle Evolution of Local Structure in Electrochemically Activated Li2MnO3. *Chem. Mater.* **2014**, *26* (24), 7091−7098.
(14) Yan, P.; Xiao, L.; Zheng, J.; Zhou, Y.; He, Y.; Zu, X.; Mao, S. X.; Xiao, J.; Gao, F.; Zhang, J.-G.; et al. Probing the Degradation Mechanism of Li2MnO3 Cathode for Li-Ion Batteries. *Chem. Mater.* **2015**, *27* (3), 975−982.
(15) Seo, D.-H.; Lee, J.; Urban, A.; Malik, R.; Kang, S.; Ceder, G. The Structural and Chemical Origin of the Oxygen Redox Activity in Layered and Cation-Disordered Li-Excess Cathode Materials. *Nat. Chem.* **2016**, *8* (7), 692−697.
(16) Luo, K.; Roberts, M. R.; Hao, R.; Guerrini, N.; Pickup, D. M.; Liu, Y.-S.; Edström, K.; Guo, J.; Chadwick, A. V.; Duda, L. C.; et al. Charge-Compensation in 3d-Transition-Metal-Oxide Intercalation Cathodes through the Generation of Localized Electron Holes on Oxygen. *Nat. Chem.* **2016**, *8* (7), 684−691.
(17) Ito, A.; Shoda, K.; Sato, Y.; Hatano, M.; Horie, H.; Ohsawa, Y. Direct Observation of the Partial Formation of a Framework Structure for Li-Rich Layered Cathode Material Li[Ni0.17Li0.2Co0.07Mn0.56]-O2 upon the First Charge and Discharge. *J. Power Sources* **2011**, *196* (10), 4785−4790.
(18) Koga, H.; Croguennec, L.; Ménétrier, M.; Douhil, K.; Belin, S.; Bourgeois, L.; Suard, E.; Weill, F.; Delmas, C. Reversible Oxygen Participation to the Redox Processes Revealed for Li1.20Mn0.54-Co0.13Ni0.13O2. *J. Electrochem. Soc.* **2013**, *160* (6), A786−A792.
(19) Koga, H.; Croguennec, L.; Ménétrier, M.; Mannessiez, P.; Weill, F.; Delmas, C.; Belin, S. Operando X-Ray Absorption Study of the Redox Processes Involved upon Cycling of the Li-Rich Layered Oxide Li1.20Mn0.54Co0.13Ni0.13O2 in Li Ion Batteries. *J. Phys. Chem. C* **2014**, *118* (11), 5700−5709.
(20) McCalla, E.; Abakumov, A. M.; Saubanère, M.; Foix, D.; Berg, E. J.; Rousse, G.; Doublet, M.-L.; Gonbeau, D.; Novák, P.; Tendeloo, G. V.; et al. Visualization of O-O Peroxo-like Dimers in High-Capacity Layered Oxides for Li-Ion Batteries. *Science* **2015**, *350* (6267), 1516−1521.
(21) Grey, C. P.; Dupré, N. NMR Studies of Cathode Materials for Lithium-Ion Rechargeable Batteries. *Chem. Rev.* **2004**, *104* (10), 4493−4512.
(22) Tran, N.; Croguennec, L.; Ménétrier, M.; Weill, F.; Biensan, P.; Jordy, C.; Delmas, C. Mechanisms Associated with the "Plateau" Observed at High Voltage for the Overlithiated Li $_{1.12}$ (Ni $_{0.425}$ Mn $_{0.425}$ Co $_{0.15}$) $_{0.88}$ O $_{2}$ System. *Chem. Mater.* **2008**, *20* (15), 4815−4825.
(23) Bareño, J.; Lei, C. H.; Wen, J. G.; Kang, S.-H.; Petrov, I.; Abraham, D. P. Local Structure of Layered Oxide Electrode Materials for Lithium-Ion Batteries. *Adv. Mater.* **2010**, *22* (10), 1122−1127.
(24) Yabuuchi, N.; Yoshii, K.; Myung, S.-T.; Nakai, I.; Komaba, S. Detailed Studies of a High-Capacity Electrode Material for Rechargeable Batteries, Li $_{2}$ MnO $_{3}$ − LiCo $_{1/3}$ Ni $_{1/3}$ Mn $_{1/3}$ O $_{2}$. *J. Am. Chem. Soc.* **2011**, *133* (12), 4404−4419.
(25) Hung, I.; Zhou, L.; Pourpoint, F.; Grey, C. P.; Gan, Z. Isotropic High Field NMR Spectra of Li-Ion Battery Materials with Anisotropy > 1 MHz. *J. Am. Chem. Soc.* **2012**, *134* (4), 1898−1901.
(26) Boulineau, A.; Simonin, L.; Colin, J.-F.; Bourbon, C.; Patoux, S. First Evidence of Manganese−Nickel Segregation and Densification upon Cycling in Li-Rich Layered Oxides for Lithium Batteries. *Nano Lett.* **2013**, *13* (8), 3857−3863.
(27) Croy, J. R.; Balasubramanian, M.; Gallagher, K. G.; Burrell, A. K. Review of the U.S. Department of Energy's "Deep Dive" Effort to Understand Voltage Fade in Li- and Mn-Rich Cathodes. *Acc. Chem. Res.* **2015**, *48* (11), 2813−2821.
(28) Dogan, F.; Long, B. R.; Croy, J. R.; Gallagher, K. G.; Iddir, H.; Russell, J. T.; Balasubramanian, M.; Key, B. Re-Entrant Lithium Local Environments and Defect Driven Electrochemistry of Li- and Mn-Rich Li-Ion Battery Cathodes. *J. Am. Chem. Soc.* **2015**, *137* (6), 2328−2335.
(29) Zheng, F.; Yang, C.; Xiong, X.; Xiong, J.; Hu, R.; Chen, Y.; Liu, M. Nanoscale Surface Modification of Lithium-Rich Layered-Oxide Composite Cathodes for Suppressing Voltage Fade. *Angew. Chem., Int. Ed.* **2015**, *54* (44), 13058−13062.
(30) Seymour, I. D.; Middlemiss, D. S.; Halat, D. M.; Trease, N. M.; Pell, A. J.; Grey, C. P. Characterizing Oxygen Local Environments in Paramagnetic Battery Materials via ^{17} O NMR and DFT Calculations. *J. Am. Chem. Soc.* **2016**, *138* (30), 9405−9408.
(31) Xiao, P.; Deng, Z. Q.; Manthiram, A.; Henkelman, G. Calculations of Oxygen Stability in Lithium-Rich Layered Cathodes. *J. Phys. Chem. C* **2012**, *116* (44), 23201−23204.
(32) Grimaud, A.; Hong, W. T.; Shao-Horn, Y.; Tarascon, J.-M. Anionic Redox Processes for Electrochemical Devices. *Nat. Mater.* **2016**, *15* (2), 121−126.
(33) Chen, H.; Islam, M. S. Lithium Extraction Mechanism in Li-Rich Li2MnO3 Involving Oxygen Hole Formation and Dimerization. *Chem. Mater.* **2016**, *28* (18), 6656−6663.
(34) Stoyanova, R.; Gorova, M.; Zhecheva, E. EPR Monitoring of Mn4+ Distribution in Li4Mn5O12 Spinels. *J. Phys. Chem. Solids* **2000**, *61* (4), 615−620.
(35) Alcántara, R.; Jaraba, M.; Lavela, P.; Tirado, J. L.; Zhecheva, E.; Stoyanova, R. Changes in the Local Structure of LiMgyNi0.5-yMn1.5O4 Electrode Materials during Lithium Extraction. *Chem. Mater.* **2004**, *16* (8), 1573−1579.
(36) Zhecheva, E.; Stoyanova, R.; Alcántara, R.; Lavela, P.; Tirado, J. L. Comparative Analysis of the Changes in Local Ni/Mn Environment in Lithium−nickel−manganese Oxides with Layered and Spinel Structure during Electrochemical Extraction and Reinsertion of Lithium. *J. Power Sources* **2007**, *174* (2), 519−523.
(37) Azamat, D. V.; Dejneka, A.; Lancok, J.; Trepakov, V. A.; Jastrabik, L.; Badalyan, A. G. Electron Paramagnetic Resonance Studies of Manganese Centers in SrTiO3: Non-Kramers Mn3+ Ions and Spin-

DOI: 10.1021/acs.jpclett.7b01425
J. Phys. Chem. Lett. 2017, 8, 4009−4016

Spin Coupled Mn4+ Dimers. *J. Appl. Phys.* **2012**, *111* (10), 104119−104125.
(38) Senguttuvan, P.; Rousse, G.; Arroyo y de Dompablo, M. E.; Vezin, H.; Tarascon, J.-M.; Palacín, M. R. Low-Potential Sodium Insertion in a NASICON-Type Structure through the Ti(III)/Ti(II) Redox Couple. *J. Am. Chem. Soc.* **2013**, *135* (10), 3897−3903.
(39) Stoyanova, R.; Ivanova, S.; Zhecheva, E.; Samoson, A.; Simova, S.; Tzvetkova, P.; Barra, A.-L. Correlations between Lithium Local Structure and Electrochemistry of Layered LiCo1−2xNixMnxO2 Oxides: 7Li MAS NMR and EPR Studies. *Phys. Chem. Chem. Phys.* **2014**, *16* (6), 2499−2507.
(40) Wandt, J.; Marino, C.; Gasteiger, H. A.; Jakes, P.; Eichel, R.-A.; Granwehr, J. Operando Electron Paramagnetic Resonance Spectroscopy − Formation of Mossy Lithium on Lithium Anodes during Charge−discharge Cycling. *Energy Environ. Sci.* **2015**, *8* (4), 1358−1367.
(41) Sathiya, M.; Leriche, J.-B.; Salager, E.; Gourier, D.; Tarascon, J.-M.; Vezin, H. Electron Paramagnetic Resonance Imaging for Real-Time Monitoring of Li-Ion Batteries. *Nat. Commun.* **2015**, *6*, 6276.
(42) Wang, Q.; Zheng, J.; Walter, E.; Pan, H.; Lv, D.; Zuo, P.; Chen, H.; Deng, Z. D.; Liaw, B. Y.; Yu, X.; et al. Direct Observation of Sulfur Radicals as Reaction Media in Lithium Sulfur Batteries. *J. Electrochem. Soc.* **2015**, *162* (3), A474−A478.
(43) Zhecheva, E.; Stoyanova, R. Effect of Allied and Alien Ions on the EPR Spectrum of Mn4+-Containing Lithium−manganese Spinel Oxides. *Solid State Commun.* **2005**, *135* (7), 405−410.
(44) Stoyanova, R.; Zhecheva, E.; Vassilev, S. Mn4+ Environment in Layered Li[Mg0.5−xNixMn0.5]O2 Oxides Monitored by EPR Spectroscopy. *J. Solid State Chem.* **2006**, *179* (2), 378−388.
(45) Gan, C.; Zhan, H.; Hu, X.; Zhou, Y. Origin of the Irreversible Plateau (4.5 V) of Li[Li0.182Ni0.182Co0.091Mn0.545]O2 Layered Material. *Electrochem. Commun.* **2005**, *7* (12), 1318−1322.
(46) Guo, J.; Cai, Y.; Zhang, S.; Chen, S.; Zhang, F. Core−Shell Structured *o* -LiMnO $_2$ @Li $_2$ CO $_3$ Nanosheet Array Cathode for High-Performance, Wide-Temperature-Tolerance Lithium-Ion Batteries. *ACS Appl. Mater. Interfaces* **2016**, *8* (25), 16116−16124.
(47) Kang, K.; Meng, Y. S.; Bréger, J.; Grey, C. P.; Ceder, G. Electrodes with High Power and High Capacity for Rechargeable Lithium Batteries. *Science* **2006**, *311* (5763), 977−980.
(48) Deng, Z. Q.; Manthiram, A. Influence of Cationic Substitutions on the Oxygen Loss and Reversible Capacity of Lithium-Rich Layered Oxide Cathodes. *J. Phys. Chem. C* **2011**, *115* (14), 7097−7103.
(49) Stoyanova, R.; Zhecheva, E.; Alcántara, R.; Tirado, J. L. Changes in Local Ni/Mn Environment in Layered LiMgxNi0.5−xMn0.5O2 (0 ≤ X ≤ 0.10) after Electrochemical Extraction and Reinsertion of Lithium. *J. Mater. Chem.* **2006**, *16* (4), 359−369.
(50) Stoyanova, R.; Barra, A.-L.; Yoncheva, M.; Zhecheva, E.; Shinova, E.; Tzvetkova, P.; Simova, S. High-Frequency Electron Paramagnetic Resonance Analysis of the Oxidation State and Local Structure of Ni and Mn Ions in Ni,Mn-Codoped LiCoO2. *Inorg. Chem.* **2010**, *49* (4), 1932−1941.
(51) Yang, J.; Guo, B.; He, H.; Li, Y.; Song, C.; Liu, G. LiNi0.5Mn0.5O2 Hierarchical Nanorods as High-Capacity Cathode Materials for Li-Ion Batteries. *J. Alloys Compd.* **2017**, *698*, 714−718.
(52) Koga, H.; Croguennec, L.; Ménétrier, M.; Mannessiez, P.; Weill, F.; Delmas, C. Different Oxygen Redox Participation for Bulk and Surface: A Possible Global Explanation for the Cycling Mechanism of Li1.20Mn0.54Co0.13Ni0.13O2. *J. Power Sources* **2013**, *236*, 250−258.
(53) Zhecheva, E.; Stoyanova, R.; Alcántara, R.; Lavela, P.; Tirado, J. L. EPR Studies of Li Deintercalation from LiCoMnO4 Spinel-Type Electrode Active Material. *J. Power Sources* **2006**, *159* (2), 1389−1394.

DOI: 10.1021/acs.jpclett.7b01425
J. Phys. Chem. Lett. 2017, 8, 4009−4016